Cambridge Centre for Computational Chemical Engineering

University of Cambridge

Department of Chemical Engineering

Preprint ISSN 1473 – 4273

A New Model For The Drying of Droplets Containing Suspended Solids

Christopher Handscomb [1] Markus Kraft [1] Andrew Bayly [2]

released: 16 July 2007

[1] Department of Chemical Engineering
University of Cambridge
New Museums Site
Pembroke Street
Cambridge, CB2 3RA
UK
E-mail: mk306@cam.ac.uk

[2] Procter and Gamble
Newcastle Technical Centre
Whitley Road
Benton
Newcastle, NE12 9TS.
UK
E-mail: a.e.bayly@pg.com

Preprint No. 50

c4e

Key words and phrases: population balance, single droplet drying, morphological development

Edited by
Cambridge Centre for Computational Chemical Engineering
Department of Chemical Engineering
University of Cambridge
Cambridge CB2 3RA
United Kingdom.

Fax: + 44 (0)1223 334796
E-Mail: c4e@cheng.cam.ac.uk
World Wide Web: `http://www.cheng.cam.ac.uk/c4e/`

Abstract

A new droplet drying model incorporating a population balance to model suspended solids is introduced. The population is evolved using a moment method with an interpolative closure employed in the case of a size dependent solids diffusion coefficient. This paper demonstrates the formulation and discusses the benefits of the new model, before presenting simulations of droplets containing colloidal silica and sodium sulphate. The results are compared with experimental data from the literature in the regime prior to shell formation.

Contents

1 Introduction

Spray drying works by contacting an atomised feed with drying air in a chamber. Unique amongst drying technologies, it combines simultaneous moisture removal with particle formation. It is the operation of choice for the industrial production of products ranging from high value pharmaceuticals to bulk commodities such as milk powder and detergents, [22]. Despite this ubiquity, spray driers still present substantial challenges to the modeller who is faced with the task of capturing complex flow fields, heat and mass transfer and morphological changes.

Integral to any detailed simulation of the spray drying process is a droplet drying submodel, [18, 26, 34]. The droplet moisture content — specifically the surface moisture — determines the rate of other processes occurring within a spray tower, such as agglomeration and wall deposition, [3, 12]. Single droplet drying models vary greatly in complexity, and many have been implemented in spray dryer simulations. The simplest approach to use is a characteristic drying curve, [5, 15, 19]. Essentially an empirical method, the approach relies upon first identifying an unhindered drying rate and then measuring a drying curve for each material considered. The reaction engineering approach introduced by Chen and Xie [4] is almost as simple and has successfully been applied to a number of spray drying systems, [5, 21]. Both methods return only particle averaged properties and give no information about morphological changes that may occur as a result of drying. More sophisticated droplet drying models are required to obtain such spatially resolved information.

Numerous spatially resolved single droplet drying models have been developed over the past 30 years. The majority of these assume that Fickian diffusion is the principle mechanism for moisture transport, [9]. Few models attempt to predict the dried particle morphology beyond the standard 'shrinking core' type analysis used by many authors, [10, 11, 17]. Sano and Keey [31] were the first to include a centrally located bubble in a drying model, thus enabling the prediction of a wider range of particle morphologies. Bubbles have since been included in models developed by Lee and Law [20] and, more recently, by Hecht and King [14]. The nature of the final particle structure is obtained in more detail by Seydel et al. [32] who employ a population balance to simulate the solid phase.

The **aim of this paper** is to introduce a new single droplet drying model which combines the best features of previously published work in this field and is thereby capable of simulating a large class of droplet drying systems. The model includes a population balance to model the nucleation and growth of suspended solids from an ideal binary solution. Further, there is provision for a centrally located bubble, thus allowing for the simulation of wet shells and puffing phenomena. This paper details the core model and presents comparisons with experimental observations of two systems prior to shell formation; details of the model formulation after shell formation, along with further applications will appear in a follow-up paper.

2 The Physics of Particle Drying

In a spray dryer, the removal of moisture from a spray of droplets involves simultaneous heat and mass transfer and, as stated above, this process is coupled to concurrent particle formation. Both the drying rate and type of particle formed depend upon the air temperature, humidity and the transport properties, in addition to the temperature, diameter and relative velocity of the drop, [29]. Typically, constant external conditions are assumed for standard single-droplet models, although this may be relaxed if, for example, the model is coupled to a CFD code to simulate the continuous phase.

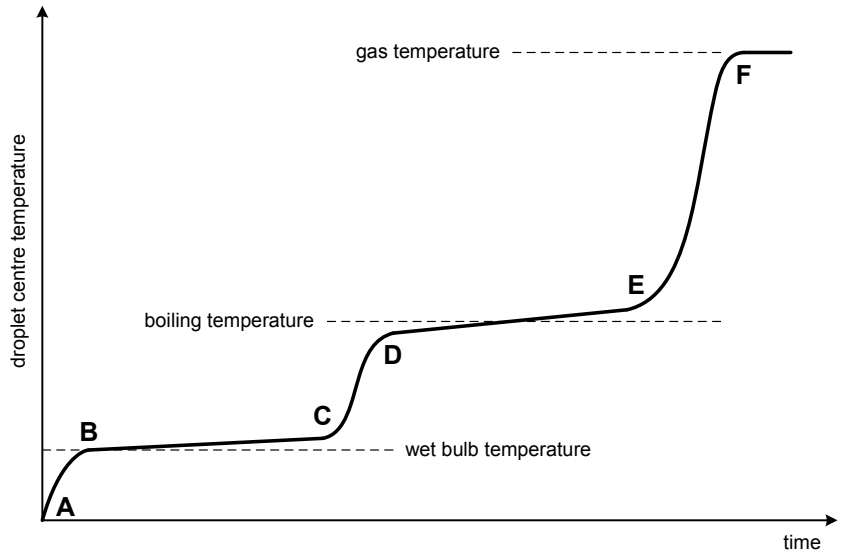

Figure 1: *The temperature history during spray drying of a liquid droplet containing suspended solids.*

Figure 1 shows a typical temperature history for an individual droplet containing dissolved or suspended solids drying in a spray tower. The droplet rapidly heats to the wet-bulb temperature, (**AB**) and then remains at the wet-bulb temperature — and drying proceeds at a near constant rate — whilst the surface remains saturated with moisture, (**BC**).

The *falling rate* or *second* drying period begins when moisture can no longer be supplied to the surface at a rate sufficient to maintain saturated conditions, (**CD**). The transition between these two regimes occurs at the *critical moisture content* and, in the presence of suspended solids, may also coincide with the start of crust formation, [6].

Vaporisation will commence if the droplet temperature reaches the moisture boiling point. Considerable energy is required for vaporisation and so the sensible heating of the droplet halts (**DE**). This phase is termed the *puffing* regime and the drying rate is now controlled by external heat transfer to the particle. Once all the free moisture has been removed, the temperature will once again rise until it equals that of the surrounding gas, (**EF**).

Numerous different particle morphologies may result when drying droplets containing dissolved or suspended solids [35], some of which are illustrated in **Figure 2**. Following crust formation, two principle pathways exist: the *dry shell* route is akin to a shrinking core producing particles which are liable to shatter if dried at high temperatures; in

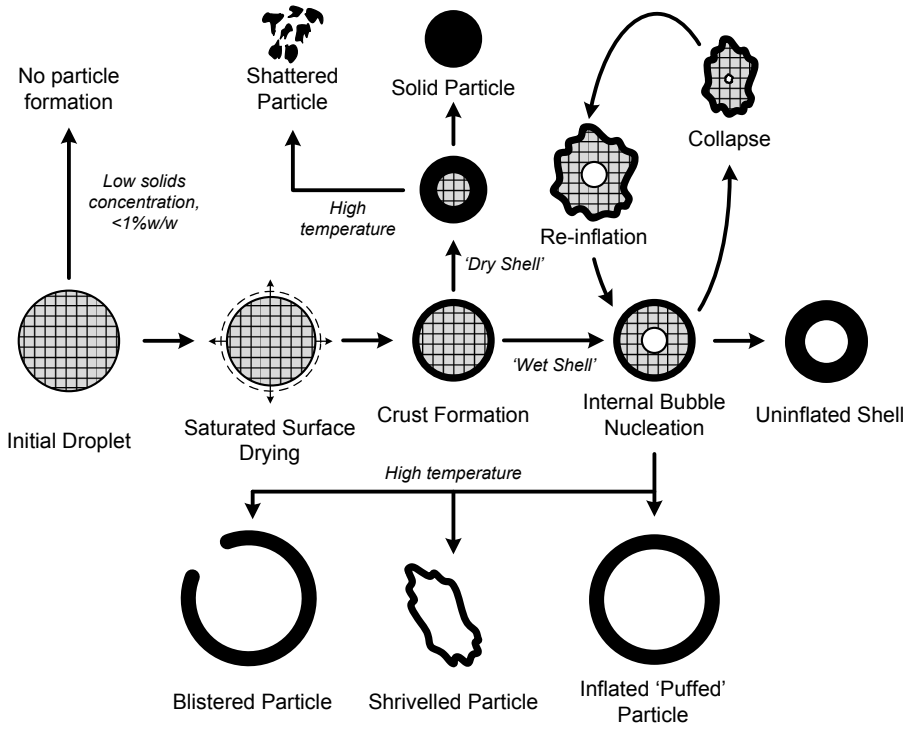

Figure 2: *Schematic showing some of the different particle morphologies that may result when drying droplets containing dissolved or suspended solids.*

contrast, particles formed by the *wet shell* route tend to be hollow and, if dried at high temperatures, inflated.

The morphology of the particles produced depends strongly on the nature of the shell formed. Previous drying models have been able to say very little about this, instead requiring the drying route to be specified from the start. The population balance in the new model provides information about the size distribution of particles forming the crust, and may thereby provide a way of *predicting* the generic morphology of the final particle.

3 Model Description

The feed to industrial spray drying units is often a complex multi-component mixture with many dissolved and suspended species. For example, a typical detergent slurry may contain between 5 and 15 separate components, [16]. In the first instance it is unrealistic to simulate such systems in their entirety; rather this paper details the development of a novel drying model incorporating three components: a solid phase and an ideal binary solution. Throughout this work, the solvent, solute and solid will be labelled A, B and D respectively.

It is assumed that the droplets maintain spherical symmetry throughout their drying history, thus reducing all equations in the final model to a single spatial dimension. Further, the Biot number is assumed low enough to justify the assumption of a spatially uniform

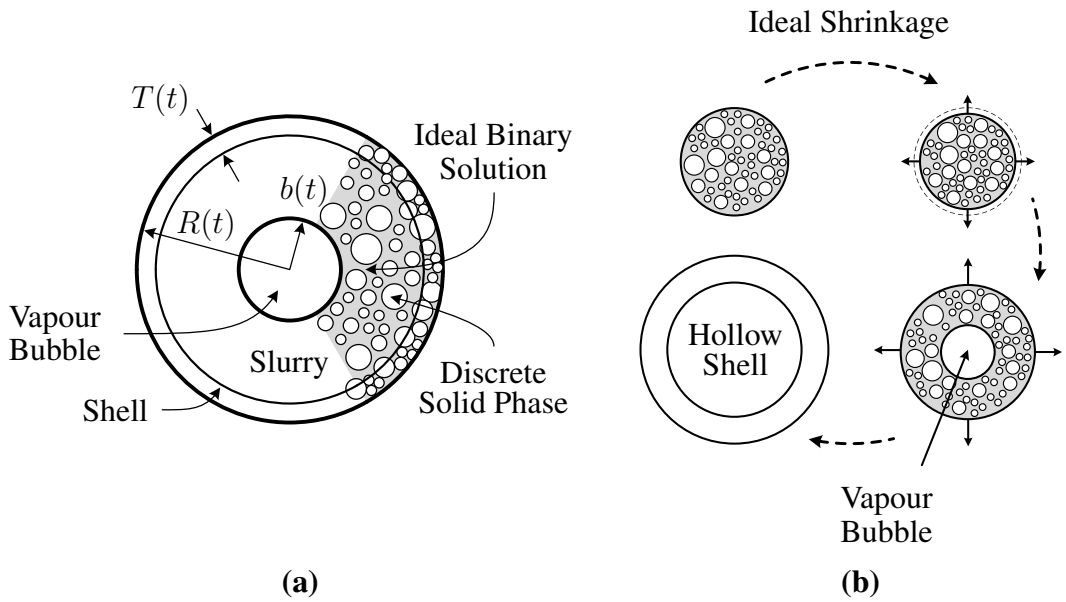

Figure 3: *Schematic showing: (a) the model system; and (b) drying to form a hollow shell.*

droplet temperature throughout the drying process. As introduced above, the new model contains a centrally located bubble and an explicit shell region, as illustrated in **Figure 3a**. One possible droplet drying history capable of being predicted by the new drying model is illustrated in **Figure 3b**.

3.1 Discrete Phase

3.1.1 Population Balance Equation

The discrete solid phase is modelled by a population of particles. These are described by a particle number density denoted $N\left(L,r,t\right)$ which evolves in time according to a population balance equation, (PBE). The particles considered in the model are assumed spherical, allowing a single internal coordinate to be used to classify particle size. The particle diameter, L, is chosen as a suitable internal coordinate, with corresponding state space $\Omega_x = [L_{\min}, \infty)$. Here $L_{\min}$ is the minimum stable crystal size which may be obtained from experimental measurements.

The velocity of motion through the state space of internal coordinates is denoted by G. The most appropriate form for G depends on the system being simulated and is obtained from experimental measurements, (see Section 4). The only assumption made at this stage that the linear growth rate is independent of crystal size, *i.e.,* $G \neq f\left(L\right)$. It is valid to approximate the linear growth rate as being independent of both particle size and the continuous phase flow where the particles are smaller than 50 μm, [24].

The assumption of spherical symmetry of the drying droplet allows a single external co-ordinate — its radial position — to completely specify the spatial location of the particle.

This external coordinate, r, has the state space $\Omega_r = [b, R]$ where b is the radius of the central bubble and R is the current droplet radius.

The solid phase may evolve in physical space through a convective or diffusive process, or a combination of the two. Incorporating this into the population balance for $N(L, r, t)$, gives the general form of the solid phase equation

$$\frac{\partial}{\partial t}N + \frac{\partial}{\partial L}(GN) + \frac{1}{r^2}\frac{\partial}{\partial r}\left(r^2 v_r^{(d)} N\right) - \frac{1}{r^2}\frac{\partial}{\partial r}\left(r^2 \mathbf{D}\frac{\partial N}{\partial r}\right) = 0\,. \tag{1}$$

In this work it is assumed that the solid particles only move through diffusion, *i.e.,* $v_r^{(d)} = 0$. Furthermore it is postulated that, once a rigid shell has formed around the droplet, the solid particles are no longer free to move at all within the shell region, *i.e.,* within a solid shell, particle growth is the sole mechanism operating.

3.1.2 Moments and Closure

Full information about the form of the number density at all times is not required; rather it is sufficient to know the local solids volume fraction, $\varepsilon(r)$. The rate of change of the solids volume fraction can be calculated from the particle number density by integrating over all particle sizes,

$$\frac{\partial \varepsilon}{\partial t} = \frac{\pi}{6}\int_{L_{\min}}^{\infty} L^3 \frac{\partial}{\partial t} N(L, r, t)\, dL = \frac{\pi}{6}\frac{\partial m_3}{\partial t}\,, \tag{2}$$

where the a^{th} integer moment *of the internal coordinate* is defined by

$$m_a(r, t) = \int_{L_{\min}}^{\infty} L^a N(r, L, t)\, dL\,. \tag{3}$$

Equation (2) shows that the evolution equation for the third moment of the number density function is required in order to compute the evolution of the solids volume fraction. To obtain this, it is necessary to derive a hierarchy of moment evolution equations by substituting (1) into (3) and differentiating.

In some applications (Section 4), a size dependent solids diffusion coefficient is required, in which case the Stokes-Einstein equation is used, leading to

$$\frac{\partial m_a}{\partial t} = -\int_{L_{\min}}^{\infty} L^a \left[G\frac{\partial N}{\partial L} - \frac{1}{r^2}\frac{\partial}{\partial r}\left(r^2 \frac{kT_d}{3\pi\mu L}\frac{\partial N}{\partial r}\right)\right] dL\,. \tag{4}$$

A nucleation condition is imposed at the lower boundary of the state space of the internal coordinate. Reduced to one dimension for crystal nucleation and growth, this gives the particle nucleation rate per unit volume, $\dot{N}_0$, as

$$\dot{N}_0 = GN(r, L_{\min}, t)\,. \tag{5}$$

Equation (4) may now be integrated, invoking standard regularity conditions, to give the general moment evolution equation,

$$\frac{\partial m_a}{\partial t} = L_{\min}^a \dot{N}_0 + aGm_{a-1} + \frac{1}{r^2}\frac{kT_d}{3\pi\mu}\frac{\partial}{\partial r}\left(r^2 \frac{\partial m_{a-1}}{\partial r}\right)\,. \tag{6}$$

In many systems, the particle inception rate, $\dot{N}_0$, will be zero and, consequently, the number density of the smallest particles will vanish. In this instance, the total number of particles in the system will not change with time.

Equation (6) does not represent a closed moment system due to the presence of the final term, arising from the use of the Stokes-Einstein relation. This term means that the evolution equation for the zeroth moment depends upon the unknown value m_{-1}. An interpolative closure [13], is employed to close this system. The closure used is based on simple linear extrapolation of the moments when plotted on a logarithmic scale. This gives

$$m_{-1} = \frac{m_0^2}{m_1} \,, \tag{7}$$

which, combined with (6) for $a \in \{0, 1, 2, 3\}$, gives a closed system of four partial differential equations for the discrete phase.

3.2 Continuous Phase equations

The continuous phase is assumed to be an ideal binary solution and consequently it is only necessary to solve for the mass fraction of one component – the solute is chosen in this work. The differential mass balance for the solute, B, in the absence of homogeneous chemical reactions is

$$\frac{\partial \rho_B}{\partial t} + \boldsymbol{\nabla} \cdot \boldsymbol{n_B} = 0 \,, \tag{8}$$

where ρ_B is the solute *bulk* density, and $\boldsymbol{n_B}$ is the mass flux of the solute relative to a fixed reference frame.

Equation (8) is sufficient to describe mass transfer in a porous medium if the configuration of the phase interfaces is known. Such a complete description is very rarely available and, even if it were, the computational time associated with such an approach would be impractical. Instead, local volume averages are introduced at each point in the structure, [33]. The aim is to associate with every point in the porous medium a local volume average of the differential mass balance for each species, (8), and hence describe the drying behaviour of the resulting homogenised medium. Such an approach has been employed by several authors to describe drying behaviour, [7, 28].

Following the notation of Slattery [33], with every point in the drying droplet, $\boldsymbol{z}$, is associated an averaging surface, S, as illustrated in **Figure 4**. Superficial and intrinsic volume averages are then defined

$$\overline{B}^{(j)} \equiv \frac{1}{V} \int_{R^{(j)}} B dV \,, \tag{9}$$

$$\langle B \rangle^{(j)} \equiv \frac{1}{V^{(j)}} \int_{R^{(j)}} B dV \,, \tag{10}$$

where B is some scalar, vector or tensor valued quantity associated with the phase j, and $R^{(j)}$ is the volume of phase j inside S. There are two phases in the present model – continuous and discrete – which are indexed by the superscripts c and d respectively.

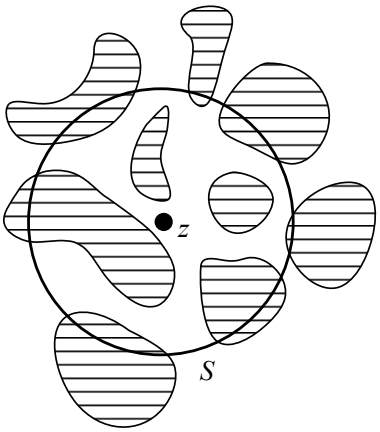

Figure 4: *Every point, $\boldsymbol{z}$, within the drying droplet has an associated averaging surface, S.*

The differential mass balance for the solute, (8), is now volume averaged to obtain

$$\frac{\partial \overline{\rho}_B^{(c)}}{\partial t} + \boldsymbol{\nabla} \cdot \overline{\boldsymbol{n}}_{\boldsymbol{B}}^{(c)} - r_B'' = 0 \,, \tag{11}$$

where r_B'' is the volume average interfacial production rate of the solute resulting from the crystallisation process. Assuming no volume change on crystallisation, r_B'' is easily obtained from the moments of the discrete phase using (6) to obtain

$$r_B'' = -\rho_D^0 \frac{\partial \varepsilon}{\partial t} = -\rho_D^0 \frac{\pi}{6} \left(L_{\min}^3 \dot{N}_0 + 3Gm_2 + \frac{1}{r^2} \frac{kT_d}{3\pi\mu} \frac{\partial}{\partial r} \left(r^2 \frac{\partial m_2}{\partial r} \right) \right) \,. \tag{12}$$

It is noted that the solids volume fraction, ε, is an inherently averaged quantity which, in the present case, is given by

$$\varepsilon = \frac{V^{(d)}}{V} = 1 - \frac{V^{(c)}}{V} \,. \tag{13}$$

Noting that $\overline{B}^{(c)} = (1-\varepsilon) \langle B \rangle^{(c)}$, and assuming that the continuous phase density, $\rho^{(c)}$, is approximately constant over the averaging volume, [38], allows (11) to be written

$$\frac{\partial}{\partial t} \left[(1-\varepsilon) \rho^{(c)} \langle \omega_B \rangle^{(c)} \right] + \boldsymbol{\nabla} \cdot \left[(1-\varepsilon) \langle \boldsymbol{n}_{\boldsymbol{B}} \rangle^{(c)} \right] - r_B'' = 0 \,, \tag{14}$$

where $\langle \omega_B \rangle^{(c)}$ is the intrinsic volume averaged solute mass fraction.

Fickian diffusion is assumed, as is common practice when analysing binary diffusion in liquids, [33]. The solute mass flux is then

$$\boldsymbol{n}_{\boldsymbol{B}} = \rho^{(c)} \omega_B \boldsymbol{v} - \mathcal{D}_{(AB)} \rho \boldsymbol{\nabla} \omega_B \,, \tag{15}$$

where $\boldsymbol{v}$ is the bulk continuous phase velocity and $\mathcal{D}_{(AB)}$ is a binary diffusion coefficient. Volume averaging this equation, following Slattery [33], and thinking of the mass flux in

terms of an effective diffusivity, $\mathbf{D}^{(e)}_{(AB)}$, gives

$$\langle \boldsymbol{n_B} \rangle^{(c)} = \rho^{(c)} \langle \omega_B \rangle^{(c)} \langle \boldsymbol{v} \rangle^{(c)} - \frac{\rho^{(c)}}{1-\varepsilon} \mathbf{D}^{(e)}_{(AB)} \cdot \boldsymbol{\nabla} \left[(1-\varepsilon) \langle \omega_B \rangle^{(c)} \right] \ . \tag{16}$$

Substituting into (14) and using the assumed spherical symmetry yields the partial differential equations used in this work to describe the evolving composition of the continuous phase

$$\begin{aligned} &\frac{\partial}{\partial t} \left[(1-\varepsilon) \rho^{(c)} \langle \omega_B \rangle^{(c)} \right] \\ &\quad + \frac{1}{r^2} \frac{\partial}{\partial r} \left[\underbrace{r^2 (1-\varepsilon) v_r^{(c)} \rho^{(c)} \langle \omega_B \rangle^{(c)}}_{\text{advection}} - \underbrace{r^2 \mathcal{D}_{\text{eff}} \rho^{(c)} \frac{\partial}{\partial r} \left[(1-\varepsilon) \langle \omega_B \rangle^{(c)} \right]}_{\text{diffusion}} \right] - r''_B = 0 \ . \end{aligned} \tag{17}$$

Here $v_r^{(c)}$ is the volume-averaged, mass-averaged radial velocity – the only non-zero component assuming spherical symmetry – and $\mathcal{D}_{\text{eff}}$ is an effective diffusion coefficient usually obtained from experiments and, in general, a function of the local moisture content.

The advective velocity in (17) arises as a result of the density difference between the solute and solvent. Considering volume conservation of the continuous phase therefore allows the following expression to be derived

$$v_r^{(c)} = \mathcal{D}_{\text{eff}} \left(\frac{1}{\Lambda_B + \langle \omega_B \rangle^{(c)}} \frac{\partial \langle \omega_B \rangle^{(c)}}{\partial r} - \frac{1}{1-\varepsilon} \frac{\partial \varepsilon}{\partial r} \right) \ , \tag{18}$$

where Λ_B is a dimensionless density ratio,

$$\Lambda_B = \frac{\rho_B^0}{\rho_A^0 - \rho_B^0} \ . \tag{19}$$

3.3 Shell and Bubble Formation

A shell is deemed to have formed once the volume fraction of particles at the droplet surface rises above a certain, predefined, value. This corresponds to the *locking* of solid particles at the surface, *i.e.,* the point at which they can no-longer freely more past each other to be drawn into the centre of the droplet. The droplet ceases to shrink at this point and, instead, a solid shell is modelled as growing inwards from the surface. The simulations presented in this paper are only run up until the point of shell formation; the details of the model beyond this point will be contained in a second paper. It is however worth noting that the information from the population balance might be used to inform the critical solids volume fraction at which shell formation is deemed to occur. For example, particles of a similar size will lock at a lower packing fraction than a population of particles with a higher variance. This is just one example of how the population balance can be used to enhance the predictive powers of the new model.

3.4 Boundary Conditions and Thermal Calculation

Water leaves the drying droplet at the surface due to a higher water activity adjacent to the droplet surface than in the bulk. In contrast, it is assumed that the solute does not leave the droplet at any time, *i.e.,* the solute mass flux following the receding interface is zero,

$$\langle n_{Br}\rangle^{(c)}\big|_{r=R(t)} = \langle n_{Br}\rangle^{(c)}\big|_{r=R} - \rho^{(c)}\langle\omega_B\rangle^{(c)}\frac{dR}{dt} = 0\,. \tag{20}$$

Substituting for the solute mass flux, (17), and rearranging gives the surface solute boundary condition

$$\left.\frac{\partial\langle\omega_B\rangle^{(c)}}{\partial r}\right|_{r=R} = \frac{\langle\omega_B\rangle^{(c)}\dot{m}_{\text{vap}}}{\rho^{(c)}\mathcal{D}_{\text{eff}}}\,, \tag{21}$$

where $\dot{m}_{\text{vap}}$, the solvent mass flux from the droplet surface, is related to the rate of shrinkage by

$$\frac{dR}{dt} = -\frac{\dot{m}_{\text{vap}}}{\rho_A^0}\,. \tag{22}$$

The solvent mass flux, $\dot{m}_{\text{vap}}$, is obtained using the algorithm suggested by Abramzon and Sirignano [1] which uses standard correlations together with film-theory based corrections for high-mass transfer rates, [2].

It is assumed that no solids leave the droplet, implying that solid particles must move towards the centre of the shrinking droplet. Physically, this is driven by the receding continuous phase menisci between solid particles. In the population balance, this is captured by means of a birth term at the boundary which, in conjunction with the expression for the diffusive volume flux from (1), gives rise to the condition

$$\left.\frac{\partial N}{\partial r}\right|_{r=R} = -\frac{\dot{m}_{\text{vap}}}{\mathrm{D}\rho_A^0}N\,. \tag{23}$$

The boundary conditions for the moments are then easily seen to be

$$\left.\frac{\partial m_i}{\partial r}\right|_{r=R} = -\frac{\dot{m}_{\text{vap}}}{\rho_A^0}\frac{3\pi\mu}{kT_d}m_{i+1} \qquad \text{for } i = 0, 1, 2\,, \tag{24}$$

$$\text{and} \quad \left.\frac{\partial\varepsilon}{\partial r}\right|_{r=R} = -\frac{\pi}{6}\frac{\dot{m}_{\text{vap}}}{\rho_A^0}\frac{3\pi\mu}{kT_d}\frac{m_3^2}{m_2} = -\frac{\dot{m}_{\text{vap}}}{\rho_A^0}\frac{18\mu}{kT_d}\frac{\varepsilon^2}{m_2}\,, \tag{25}$$

where the interpolation $m_4 = m_3^2/m_2$ has been used in the last equation to close the system.

Symmetry implies zero gradient boundary conditions should be employed at the centre of the droplet until the formation of a central bubble.

The algorithm given in Abramzon and Sirignano [1] is also used to calculate the heat penetrating into the drying droplet. From this — and the assumption of no internal temperature gradients — the droplet temperature is evolved. The incorporation of this algorithm was tested by simulating the evaporation of a pure water droplet and comparing predicted mass and temperature histories with those measured by Werner [36], (**Figure 5**).

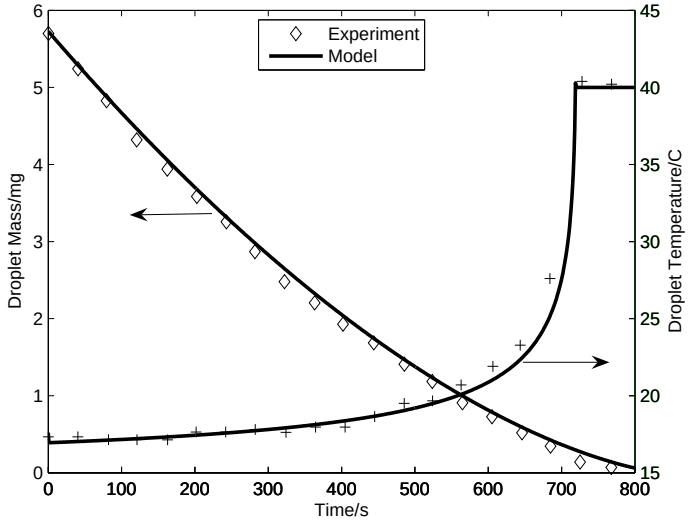

Figure 5: *Comparison of simulated and measured mass and temperature profiles for the evaporation of a pure water droplet. Experimental data is taken from Werner [36] and refers to a 6 μl droplet drying in air at 40°C, 3.75% relative humidity and flowing with a velocity of 0.3 ms^{-1}.*

4 Implementation and Results

The model as described consists of a set of advection-diffusion equations coupled to ordinary differential equations describing the particle size and temperature. These were solved using the standard NAG Fortran `D03PFF` library routine, [NAG], which implements an algorithm developed by Pennington and Berzins [27] when supplied with a user-defined switching-upwind numerical flux function.

4.1 Coordinate System Normalisation

The physical extent of the droplet changes during drying due to both shrinkage and, although not discussed in this paper, bubble growth. The situation is further complicated if a shell has formed, as this has an additional associated coordinate system whose extent also varies with time. To handle the resulting moving boundary problem, the following coordinate transformation is applied to all equations,

$$z = \frac{r - r_{\mathrm{L}}}{r_{\mathrm{R}} - r_{\mathrm{L}}} \quad ; \quad \frac{\partial}{\partial r} = \frac{1}{r_{\mathrm{R}} - r_{\mathrm{L}}} \frac{\partial}{\partial z} \, , \tag{26}$$

where, $[r_{\mathrm{L}}, r_{\mathrm{R}}] = [b, S]$ for the internal coordinate system and $[r_{\mathrm{L}}, r_{\mathrm{R}}] = [S, R]$ for the shell region. This transformation has the effect of non-dimensionalising the spatial coordinate and fixing both internal and shell domains on the interval $z \in [0, 1]$. Time derivatives in the z coordinate systems are related to those in the r coordinate system by

$$\left.\frac{\partial}{\partial t}\right|_r = \left.\frac{\partial}{\partial t}\right|_z - \frac{1}{R_0}\left[\frac{dr_{\mathrm{L}}}{dt} + z\frac{dR_0}{dt}\right]\frac{\partial}{\partial z} \, , \tag{27}$$

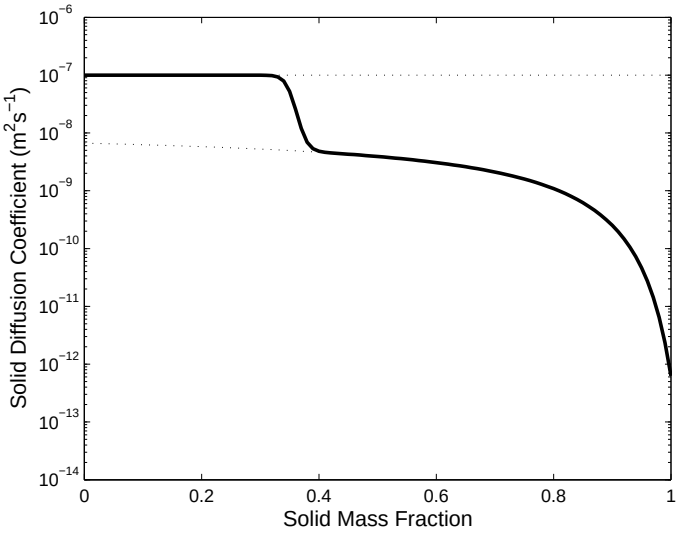

Figure 6: *Plot of the solids diffusion coefficient used to simulate the drying of a colloidal silica droplet.*

where $R_0 = r_{\mathrm{R}} - r_{\mathrm{L}}$. The transformation is seen to add a virtual flux to all the partial differential equations in the model.

4.2 Drying a Droplet Containing Colloidal Silica

The first test case simulated is the drying of a colloidal silica droplet containing 16nm particles suspended in water at an initial mass fraction of 30%. To simulate this system using the current model the solute mass fraction is initialised to a very small number, 10^{-9}, thus approximating the pure water continuous phase. The simulation results prior to shell formation are then compared with experimental results from Nesic and Vodnik [25] at two different drying air temperatures.

Colloidal silica forms a gel at mass fractions above 40%. Nesic and Vodnik [25] report the solids diffusion coefficient in this gel phase as

$$\mathrm{D} = \exp\left(\frac{28.1 + 282\,(1-\varepsilon)}{1 + 15.47\,(1-\varepsilon)}\right) \ . \tag{28}$$

In this example, a size dependent diffusion coefficient is not employed — there is only one particle size — and consequently the closure discussed in Section 3.1.2 is not required.

Prior to gel formation, experimental observations suggest that internal convection currents keep the drying droplets well mixed. To simulate this, the diffusion coefficient, (28), is set to 10^{-7} m^{2}s^{-1} – a relatively large value – at low solids concentrations. This gives the functional form for the diffusion coefficient shown in **Figure 6**, where the discontinuity at the point of gel formation has been removed through use a hyperbolic tangent weighting function.

Direct comparisons with the experimental data at $T_{\text{gas}} = 101°$C and $T_{\text{gas}} = 178°$ C are presented in **Figure 7 (a)** and **(b)** respectively. A shell was deemed to have formed once the solids volume fraction at the surface of the droplet exceeded 0.65, at which point the simulation terminated. As can be seen from the figures, shell formation is predicted at $t = 60$ s when drying at $101°$C and at $t = 32$ s at the higher temperature. This is slightly earlier than the experimental observations, possibly indicating that a more sophisticated shell initiation model is required. Prior to shell formation, the agreement with observations is good.

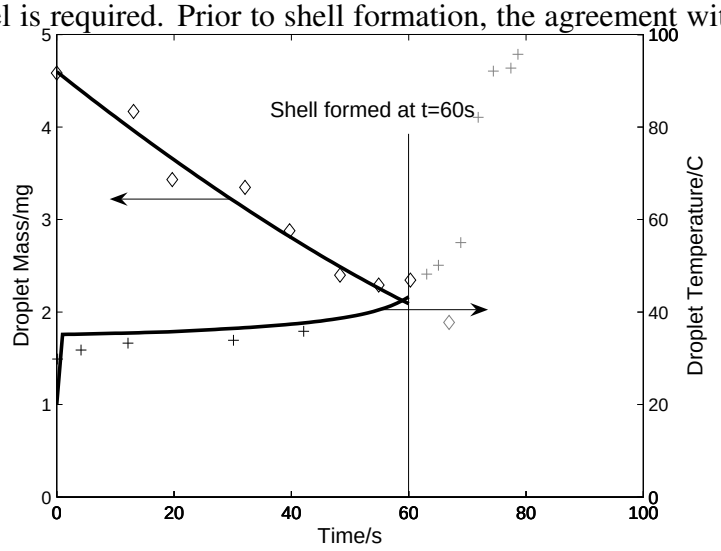

(a)

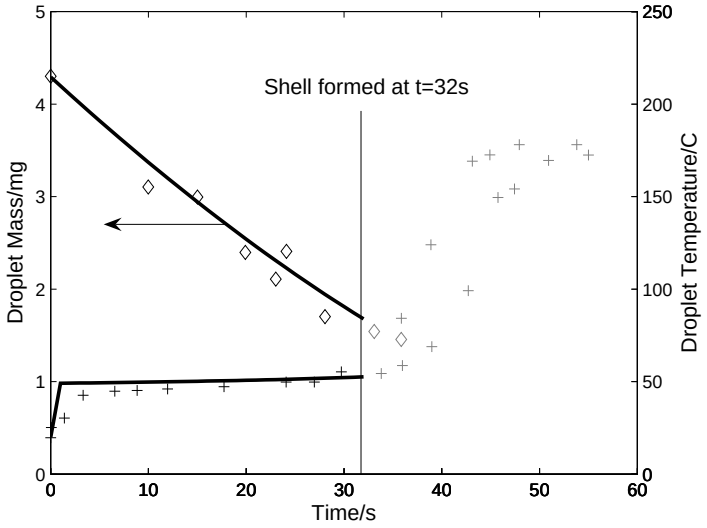

(b)

Figure 7: *Simulated drying of a colloidal silica droplet (lines) compared with experimental results from Nesic and Vodnik [25] (points) at: (a) $T_{\text{gas}} = 101°$ C and $v = 1.73$ ms^{-1}; and (b) $T_{\text{gas}} = 178°$ C and $v = 1.4$ ms^{-1}. RH=3.75% in both cases.*

Figure 8 shows the predicted evolution of the solids volume fraction within the colloidal silica droplet drying at $T_{\text{gas}} = 101°$ C. Profiles are plotted at 5 s intervals. Initially the

profiles are flat across the droplet due to internal circulation prior to the formation of the gel phase. After formation of a gel at $\varepsilon = 0.233$, the profiles develop a pronounced curvature as particles build up at the receding interface. In the current model, shell formation is predicted when the surface solid volume fraction reaches 0.65, which is seen to occur at $t = 60$ s.

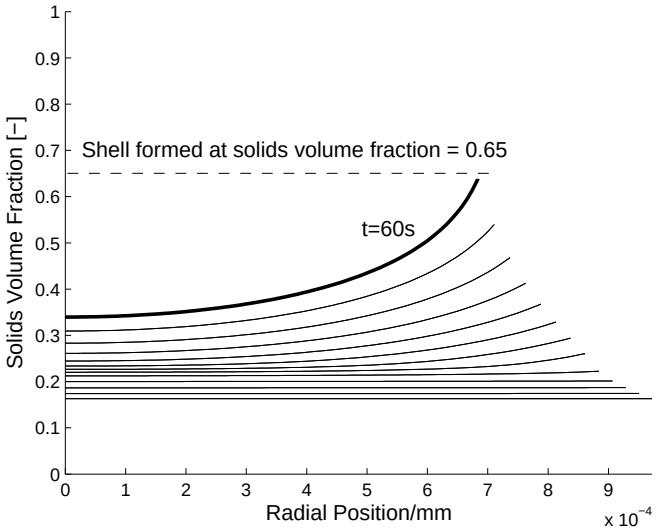

Figure 8: *Simulated solids volume fraction profiles during the drying of a colloidal silica droplet in air at $T_{\text{gas}} = 101°C$. Profiles plotted at 5s intervals, with shell formation predicted at $t = 60$s, (highlighted).*

4.3 Drying a Sodium Sulphate Droplet

The second set of results presented relate to the drying of a droplet of sodium sulphate solution. The droplet simulated has an initial solute content of 14wt%, which is just below saturation at the initial droplet temperature of 20°C . The model is initialised with a uniform solids volume fraction of 1.1×10^{-12} which corresponds to a total of 100 crystal nuclei with diameter of 400 nm in the initial droplet.

Above 30°C, sodium sulphate solution crystallises directly to solid sodium sulphate without forming a hydrated phase, [37]. The drying droplet rapidly achieves a wet bulb temperature in excess of 30°C and so the kinetics used are those for direct crystallisation to the solid, and are taken from Rosenblatt et al. [30],

$$\frac{dL}{dt} = 1.484 \times 10^7 \exp\left(-\frac{13.7 \times 10^3}{RT}\right)(C_{\text{i}} - C_{\text{eqm}})^{1.5} \ , \tag{29}$$

which corresponds to the linear growth rate, G/ms^{-1}, in the population balance equation (1). C_{i} and C_{eqm} are the local and saturated solute concentrations respectively in kmolm^{-3}. The saturation ratio, S, is less than 5 throughout drying so heterogeneous nucleation dominates. The following function was used for the heterogeneous nucleation

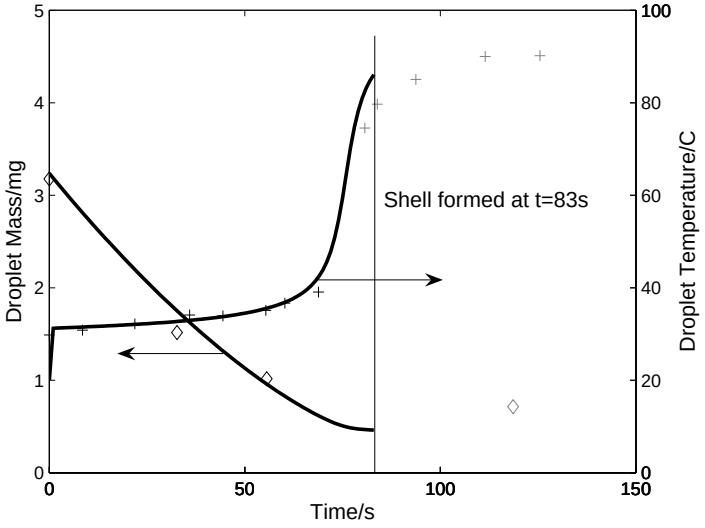

Figure 9: *Simulated drying of a 14wt% sodium sulphate in water droplet at* $T_{\mathrm{gas}} = 90\,^{\circ}C$*, compared with experimental results from Nesic and Vodnik [25].*

rate

$$\log\left(\frac{\dot{N}_0}{10^{11}}\right) = \frac{-2}{\log^2(S)}\,, \tag{30}$$

which is taken from Dirksen and Ring [8] and relates to similar systems.

The binary diffusion coefficient of the solute is estimated using the Wilke-Chang correlation to be 2.6 $\mathrm{m^2 s^{-1}}$ at 293 K. From this, the effective diffusion coefficient used in (17), taking account of the solid phase, is obtained very approximately using the Clausius-Mossotti model. Raoult's law is used to obtain the moisture vapour pressure above the surface of the drying droplet.

Comparisons with experimental measurements from Nesic and Vodnik [25] of a sodium sulphate droplet drying in air at 90° C are presented in **Figure 9**. The agreement of the total droplet mass and temperature profiles prior to shell formation is good. Again taking the trigger for shell formation to be a surface solids volume fraction of 0.65, it is seen that a rigid crust is predicted at 83 s. Under these conditions it is apparent that the shell forms rather late in the droplet drying history at a point where the droplet temperature has already risen substantially due to concentration of the solute at the surface.

Figure 10 plots the solute mass fraction profiles at 5 s intervals through the drying of the droplet. The dashed curve is the solute profile at the point of shell formation and the lower highlighted curve indicates the first profile where the solution throughout the droplet becomes supersaturated. This point coincides with the rapid increase in the number of crystals, which is seen clearly in **Figure 11**. This figure shows the moments integrated over the external coordinate and normalised using

$$\tilde{M}_i = \frac{4\pi}{m_i(0)\,V_0}\int_b^R r^2 m_i dr\,. \tag{31}$$

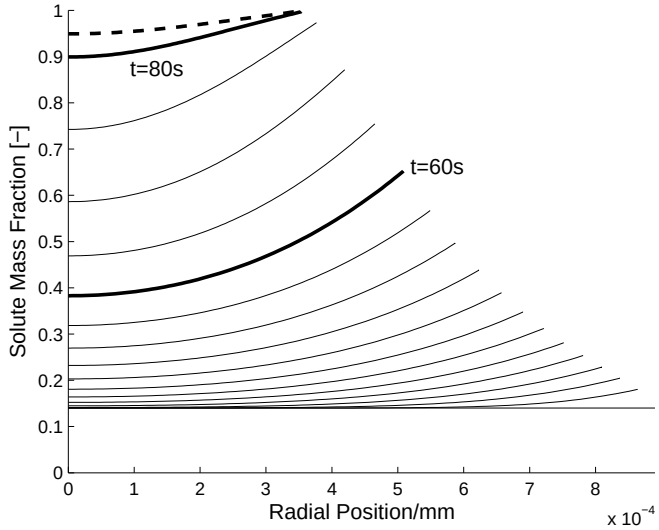

Figure 10: *Simulated solute mass fraction profiles plotted at 5 s intervals throughout the drying of a droplet of aqueous sodium sulphate solution, and at the point of shell formation (dashed line).*

The normalised moments are coincident during most of the droplet drying history. This is to be expected because nucleation dominates over growth throughout most of the drying period.

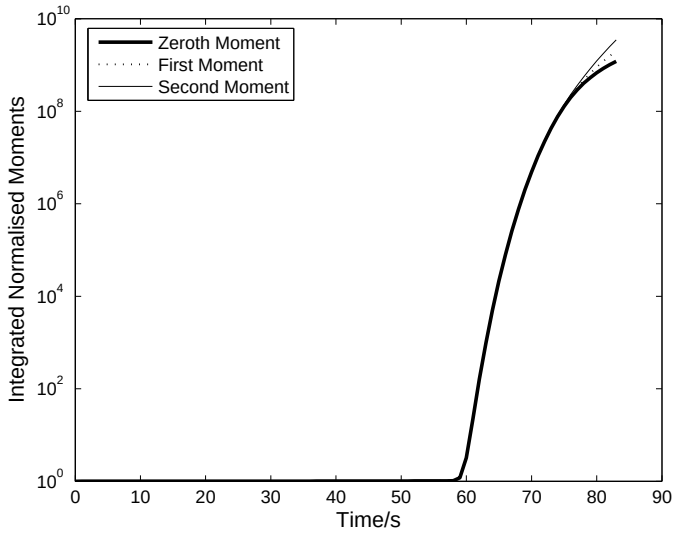

Figure 11: *Simulated normalised moments integrated over the external coordinate.*

The zeroth moment gives the total number of solid particles in the drying system, and this is seen to increase rapidly after about 60 s. **Figure 12** shows radial profiles of the zeroth moment plotted at 5 s intervals. Prior to the 60 s curve, (highlighted), the moment value only increases due to shrinkage of the droplet influencing the initial seed distribution.

The behaviour after 60 s is seen to be quite different, with the number density increasing markedly, eventually across the whole of the droplet. Closer inspection shows the curves have a steeper gradient adjacent to the surface of the droplet. This reflects the effect of the size dependent diffusion coefficient; the first moment of the particle size distribution shows that the particles are larger close to the surface, as would be expected of the oldest particles.

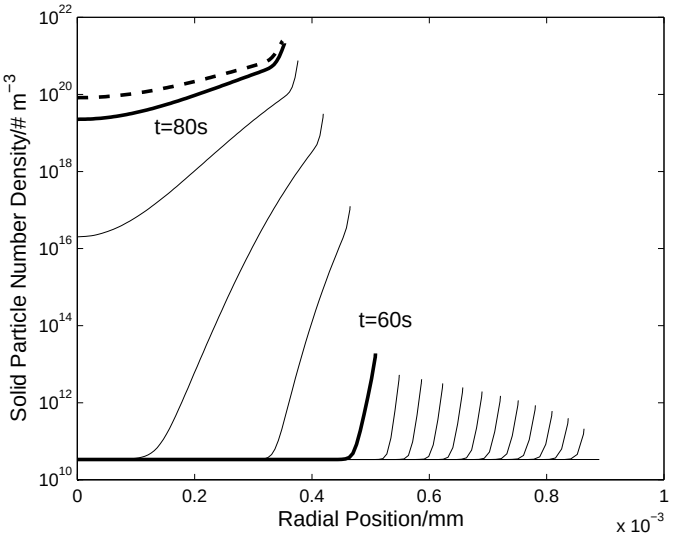

Figure 12: *Simulated particle number density in a drying droplet of aqueous sodium sulphate solution. Profiles plotted at 5s intervals and on shell formation (dashed) at* $t = 83s$.

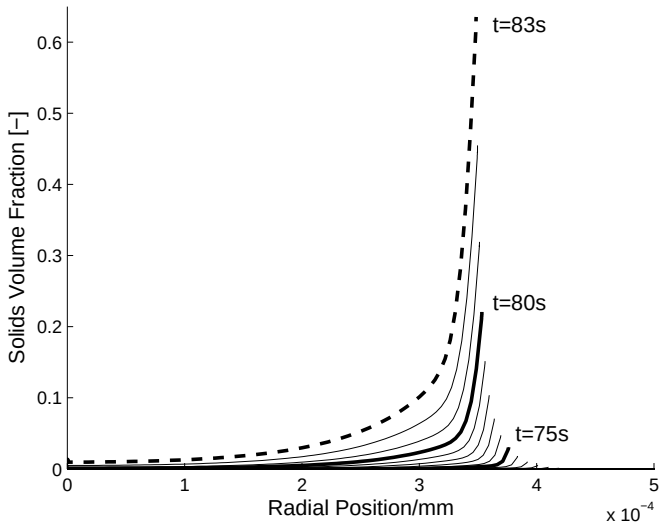

Figure 13: *Simulated solids volume fraction in a drying droplet of aqueous sodium sulphate solution.*

Figure 13 shows the predicted evolution of the solids volume fraction in the drying droplet. The volume fraction of solids is negligible until $t = 72$ s, despite the increase in the moment values from around $t = 60$ s. However, beyond $t = 72$ s the solids volume fraction at the droplet surface rises rapidly as result of continued crystallisation and shrinkage of the droplet. The rate of increase is then such that a shell is then formed in 11 s.

The kinetics of the crystal nucleation and growth processes are key in determining the timing of shell formation in this system. The increase in the moments at $t = 60$ s noted in **Figure 11** is so timed as a result of the expression for the nucleation rate, (30). The relative rates of nucleation and growth then set the time taken for shell formation. The population balance for the solid phase is therefore critical for accurate modelling of this system.

5 Conclusions

This paper has introduced a new model to simulate the drying of droplets comprising an ideal binary solution with suspended solids. The model has been developed to enable prediction of dried particle morphologies, together with the droplet drying rate. The key to achieving structural prediction is the incorporation of a population balance to model the solid phase within the drying droplet. This population balance admits particle nucleation and growth, together with an external coordinate to describe the radial location within the drying droplet. The model solves for the first four moments of this population, from which the local solids volume fraction and other quantities of interest can be deduced.

Although not discussed in this paper, the model has been extended to include a central bubble and shell formation, details of which will be presented in a future paper. These two features are the remaining pieces required to simulate a wide range of particle morphologies. The use of a population balance is essential to this prediction, extending the capabilities of this model far beyond those of existing approaches. The average local size and variance of the particles, for example, allows the critical solids volume fraction at which the shell forms to be determined; a shell formed from particles with a similar diameter will have a higher porosity than one comprised of particles of different sizes. Beyond this, the information gained from the population balance might be used to give an idea of the structural properties of the shell, which will be critical in predicting its morphological response to further drying or bubble growth.

Two simulations have been presented in this paper validating the new model up to the point of shell formation. The results illustrate the information — moments, solute profiles, droplet temperature and size — made available by the new model and confirm that this is a promising approach.

Nomenclature

Greek symbols

Ω_r	State space of the external coordinate
Ω_x	State space of the internal coordinate
ε	Solids volume fraction
μ	Viscosity
ω	Mass fraction
ρ	Bulk density
ρ^0	Bulk density

Roman symbols

C	Molar concentration
$\mathcal{D}_{\text{eff}}$	Effective diffusion coefficient
D	Solids diffusion coefficient
G	Linear growth rate
L	Internal coordinate - particle diameter
$L_{\min}$	Minimum stable crystal size
$\dot{N}_0$	Particle nucleation rate
N	Number density function
R	Radius of the drying droplet
R	Gas constant
R_0	Physical extent of the domain
S	Saturation ratio
V	Volume
V_o	Initial droplet volume
b	Radius of the central bubble
T_d	Droplet temperature
k	Boltzmann constant

m_a a$^{\text{th}}$ integer moment of the internal coordinate

$\dot{m}_{\text{vap}}$ Mass vapour flux from the droplet

$\boldsymbol{n}$ Mass flux with respect to a stationary reference frame

n_r Radial mass flux

r Internal coordinate - radial position

t Time

v_r Radial velocity

$v_r^{(c)}$ Volume averaged continuous phase radial velocity

z Non-dimensionalised spatial coordinate

Operators

$\overline{B}^{(j)}$ Superficial volume average of B associated with phase j

$\langle B \rangle^{(j)}$ Intrinsic volume average of B associated with phase j

Superscripts and Subscripts

A Solvent

B Solute

D Solids

c Continuous phase

d Discrete phase

References

[1] B. Abramzon and W. A. Sirignano. Droplet vaporization model for spray combustion calculations. *Int J Heat Mass Tran*, 32:1605–1618, 1989.

[2] R. B. Bird, W. E. Stewart, and E. N. Lightfoot. *Transport Phenomena*. John Wiley and Sons, 1st edition, 1960.

[3] S. Blei and M. Sommerfeld. Consideration of particle interactions in spray dryer modelling: An extended euler-lagrange approach. In *Proceedings of the 15th International Drying Symposium (IDS 2006)*, pages 307–314, August 2006.

[4] X. Chen and G. Xie. Fingerprints of the drying behaviour of particulate or thin layer food materials established using a reaction engineering model. *T I Chem Eng-Lond*, 75(C):213–222, 1997.

[5] X. D. Chen and S. X. Q. Lin. The reaction engineering approach to modelling drying of milk droplets. *Proceedings of the 14th International Drying Symposium*, C:1644–1651, August 2004.

[6] H. Cheong, G. Jeffreys, and C. Mumford. A receding interface model for the drying of slurry droplets. *A. I. Ch. E.*, 32(8):1334–1346, August 1986.

[7] A. A. U. de Souza and S. Whitaker. The modelling of a textile dyeing process utilizing the method of volume averaging. *Braz J Chem Eng*, 20(4):445–453, October-December 2003.

[8] J. A. Dirksen and T. A. Ring. Fundamentals of crystallization: Kinetic effects on particle size distributions and morphology. *Chem Eng Sci*, 46(10):2389–2427, 1991.

[9] G. I. Efremov. Drying kinetics derived from diffusion quation with flux-type boundary conditions. *Dry Technol*, 20(1):55–66, January 2002.

[10] T. Elperin and B. Krasovitov. Evaporation of liquid droplets containing small solid particles. *International Journal of Heat and Mass Transfer*, 38(12):2259–2267, 1995.

[11] M. Farid. A new approach to modelling of single droplet drying. *Chem Eng Sci*, 58: 2985–2993, 2003.

[12] D. Fletcher, B. Guo, D. Harvie, T. Langrish, J. Nijdam, and J. Williams. What is important in the simulation of spray dryer performance and how do current cfd models perform? In *Third International Conference on CFD in the Minerals and Process Industries*, pages 357–364. CSIRO Australia, CSIRO Australia, December 2003.

[13] M. Frenklach. Method of moments with interpolative closure. *Chem Eng Sci*, 57 (12):2229–2239, 2002.

[14] J. P. Hecht and C. J. King. Spray drying: Influence of developing drop morphology on drying rates and retention of volatile substances. 2. modeling. *Ind Eng Chem*, 39: 1766–1774, 2000.

[15] L. Huang, K. Kumar, and A. S. Mujumdar. Computational fluid dynamic simulation of droplet drying in a spray dryer. *Proceedings of the 14th International Drying Symposium*, A:326–332, August 2004.

[16] D. H. Huntington. The influence of the spray drying process on product properties. *Dry Technol*, 22(6):1261–1287, 2004.

[17] M. Kadja and G. Bergeles. Modelling of slurry droplet drying. *Appl Therm Eng*, 23: 829–844, 2003.

[18] T. Langrish and D. Fletcher. Prospects for the modelling and design of spray dryers in the 21st century. *Dry Technol*, 21(2):197–215, 2003.

[19] T. Langrish and T. Kockel. The assessment of a characteristic drying curve for milk powder for use in computational fluid dynamics modelling. *Chem Eng J*, 84:69–74, 2001.

[20] A. Lee and C. Law. Gasification and shell characteristics in slurry droplet burning. *Combust Flame*, 85(1):77–93, 1991.

[21] S. X. Q. Lin and X. D. Chen. Prediction of air-drying of milk droplet under relatively high humidity using the reaction engineering approach. *Dry Technol*, 23(7):1395–1406, 2005.

[22] K. Masters. *Spray Drying Handbook*. Longman Scientific and Technical, UK, 5th edition, 1992.

[23] *NAG Fortran Library Routine Document: D03PFF*. NAG, (Numerical Algorithms Group).

[24] S. Nagata. *Mixing: Principles and Applications*. Kodansha Scientific Books. Tokyo: Kodansha, 1st edition, 1975. a Halsted Press book.

[25] S. Nesic and J. Vodnik. Kinetics of droplet evaporation. *Chem Eng Sci*, 46(2): 527–537, 1991.

[26] D. E. Oakley. Spray dryer modeling in theory and practice. *Dry Technol*, 22(6): 1371–1402, 2004.

[27] S. V. Pennington and M. Berzins. New nag library software for first-order partial differential equations. *ACM T Math Software*, 20(1):63–69, March 1994.

[28] G. O. Porras, F. Couture, and M. Roques. An eulerian convection-diffusion model for convection drying of a deformable media composed of a binary liquid. In *Proceedings of the 15th International Drying Symposium (IDS 2006)*, pages 299–306, August 2006.

[29] W. Ranz and W. Marshall. Evaporation from drops. *Chem Eng Prog*, 48(141):173, 1952.

[30] D. Rosenblatt, S. B. Marks, and R. L. Pigford. Kinetics of phase transitions in the system sodium sulfate-water. *Ind End Chem*, 23(2):143–147, May 1984.

[31] Y. Sano and R. Keey. The drying of a spherical partical containing colloidal material into a hollow sphere. *Chem Eng Sci*, 37(6):2985–2993, 1982.

[32] P. Seydel, J. Bl omer, and J. Bertling. Modeling particle formation at spray drying using population balances. *Dry Technol*, 24(2):137–146, 2006.

[33] J. C. Slattery. *Advanced Transport Phenomena*. Cambridge Series in Chemical Engineering. Cambridge University Press, 1st edition, 1999.

[34] R. Verdurmen, P. Menn, J. Ritzert, S. Blei, G. Nhumaio, T. S. Sorensen, M. Gunsing, J. Straatsma, M. Verschueren, M. Sibeijn, G. Schulte, U. Fritsching, K. Bauckhage, C. Tropea, and M. Sommerfeld. Simulation of agglomeration in spray drying installations: The edecad project. *Dry Technol*, 22(6):1403–1461, 2004.

[35] D. Walton and C. Mumford. Spray dried products - characterization of particle morphology. *T I Chem Eng-Lond*, 77(A):21–37, January 1999.

[36] S. R. L. Werner. *Air Suspension Coating of Dairy Powders: a Micro-Level Process Approach*. PhD thesis, Massey University, Palmerston North, New Zealand, 2005.

[37] F. E. W. Wetmore and D. J. LeRoy. *Principles of Phase Equilibria*. International Chemical Series. McGraw-Hill, 1st edition, 1951.

[38] S. Whitaker. The equations of motion in porous media. *Chem Eng Sci*, 21:291–300, 1966.